Available online at www.sciencedirect.com
ScienceDirect
Additive Manufacturing 6 (2015) 39–52
Additive MANUFACTURING
www.elsevier.com/locate/addma

Intra-layer closed-loop control of build plan during directed energy additive manufacturing of Ti–6Al–4V

Abdalla R. Nassar*, Jayme S. Keist[1], Edward W. Reutzel[2], Todd J. Spurgeon

Applied Research Laboratory, The Pennsylvania State University, University Park, PA 16804, USA

Accepted 17 March 2015
Available online 25 March 2015

Abstract

The location, timing, and arrangement of depositions paths used to build an additively manufactured component – collectively called the build plan – are known to impact local thermal history, microstructure, thermal distortion, and mechanical properties. In this work, a novel system architecture for intra-layer, closed-loop control of the build plan is introduced and demonstrated for directed-energy deposition of Ti–6Al–4V. The control strategy altered the build plan in real time to ensure that the temperature around the start point of each hatch, prior to deposition, was below a threshold temperature of 415 °C. Potential hatches with an initial temperature above this threshold were temporarily skipped. Compared with open-loop processing, closed-loop control resulted in vertical alignment of columnar prior-β grains, more uniform α-lath widths, and more-uniform microhardness values within the deposited component.

Keywords: Additive manufacturing; Directed energy deposition; Control; Ti–6Al–4V; Lath width; Hardness

1. Introduction

Additive Manufacturing (AM) of metal-based components has recently garnered increasing attention. This interest is motivated by the potential to inexpensively and rapidly produce or repair high-value, complex parts. The novel capabilities offered by AM, however, come at an expense. Manufacturing of even simple components via AM is complex, typically requiring hundreds or thousands of individual laser or electron-beam depositions. The ordering, timing, and placement of depositions, also known as a hatch plan, path plan, or build plan, define a part's thermal history throughout the build. As is discussed in Section 1.1, this affects part microstructure, residual stresses, distortion, and mechanical properties.

1.1. Influence of build plan on microstructure and properties

Previous researchers have investigated the effects of build plan on microstructure and properties primarily using one of the two strategies. Following the first strategy, changes in microstructure and properties as a result of changing build orientation are investigated. Due to the greater flexibility in depositing overhangs, this approach is typically limited to powder-bed fusion (PBF) processes. Following the second approach, investigators examine the effects of location, order and timing of deposition paths on microstructure and mechanical properties.

To assess the effect of part orientation – and hence the build plan – researchers have built geometrically simple parts, such as cylindrical or flat tensile specimens, with their major axis oriented at various angles with respect to the build-up (z-axis) direction [1–3]. For example, Tolosa et al. [3] used a laser-based, BPF process to deposit flat AISI 316L stainless steel tensile and Charpy impact test specimens oriented at angles of 0°, 45°,60°, and 90° with respect to the build-up direction. Additionally, the

* Corresponding author. Tel.: +1 814 863 9409; fax: +1 814 863 1183.
E-mail addresses: arn5000@psu.edu (A.R. Nassar), jsk25@psu.edu (J.S. Keist), ewr101@arl.psu.edu (E.W. Reutzel), tjs@vt.edu (T.J. Spurgeon).
[1] Tel.: +1 814 867 4785.
[2] Tel.: +1 814 863 9891.

http://dx.doi.org/10.1016/j.addma.2015.03.005
2214-8604/

orientation of the flat-edge of the tensile samples and the rotation angle on the build plate were investigated. Differences in tensile strength, yield strength, and elongation percent were observed; however, explanations for this were not provided. Samples oriented parallel to the build-up direction exhibited the largest values for elongation percentage, while samples oriented perpendicular to the build-up direction, with the flat edge of the tensile sample laying on the build plate, exhibited largest values for yield and ultimate strength.

Similar patterns have been observed during electron beam PBF of Ti–6Al–4V using the Arcam EBM® process: tensile specimens showed larger elongation percentage for orientations parallel to the build-up direction and higher yield and ultimate strength when oriented perpendicular to the build-up direction [1,2]. Rafi et al. suggested that such differences might be due to defects along planes perpendicular to the build-up direction, inter-granular discontinuities, or differences in α-lath widths. The pattern observed by Tolsoa et al., Rafi et al., and Brandl et al. is, however, contradicted by the observations of Hrabe and Quinn [4]; they reported a higher elongation percentage and lower strength for Ti–6Al–4V samples deposited perpendicular to the build-up direction using the Arcam EBM® process. Though the results were attributed to the texture and elongation of the prior-β grains and reference was made to a previous study drawing similar conclusions [5], why results differed from studies [1,2], which employed similar AM technologies and analysis techniques, is unclear.

It is also unclear how mechanical properties such as indentation hardness are affected by orientation. On the one hand, Tolosa et al. [3] have suggested that hardness profiles of AM parts built using laser-based PBF are uniform and have mechanical properties comparable to wrought components irrespective of orientation. On the other hand, Roy [6] reported higher nanoindentation hardness values for electron-beam-PBF-deposited, Ti–6Al–4V tensile samples oriented perpendicular to the build-up direction than those oriented parallel to it.

Despite lack of a clear explanation for how part orientation in powder-bed systems impacts properties, its impact on microstructure is better understood. In Ti–6Al–4V, the ⟨0 0 1⟩ direction of β grains preferentially aligns parallel to the maximum thermal gradient [7,8]. Altering a part's build plan or part dimensions has been shown to alter prior-β grain orientation in Ti–6Al–4V [8]. Alternating layer-to-layer scan direction during selective laser melting has also been shown to result in a "herringbone pattern" [9,10].

Similar effects were found using directed-energy depositions (DED) of Ti–6Al–4V. Using a tungsten inert cast (TIG) welding system, Baufeld [11] showed that prior-β grains were slanted along the temperature gradient. This was previously observed with laser-based, DED processes [12]. The effect of build plan on microstructure has also been observed in other alloy systems. For instance, for powder-feed DED of Inconel 625, Dinda et al. [13] showed that alternating layer-to-layer scan direction rotated the growth direction of columnar dendrites by 90° from layer-to-layer. Though build plan impacts microstructure, properties and thermal stress, the authors are unaware of any efforts toward closed-loop control of build plan.

1.2. Control of AM

Much work on closed-loop control of AM processes has been performed. Most researchers focus on real-time control of the deposition process by varying the laser power or processing speed based on sensing of the melt pool size [14–18] or temperature [19,20]. Some have also attempted to maintain a constant working distance, or layer build height, by sensing the build height and adjusting the processing head position [21], the processing speed [22,23], the filler material feed rate [24] or the laser power [25]. Another target of closed-loop control efforts is varying powder or wire-feed rates to control material composition for functionally graded materials deposition [26,27]. For reviews of in-process monitoring and control for AM, see [28–31].

Here, we depart from efforts using real-time control of one or multiple variables and instead investigate closed-loop control of the build plan during directed-energy AM. A system architecture was developed to enable intra-layer build-plan modification, based on measurement of the local, initial temperature of each potential deposition path, also referred to as hatch, on a layer. We found that closed-loop control of the order and timing of hatches, based on their initial temperature, affected the microstructure and properties of deposited parts. Closed-loop control resulted in vertical alignment of columnar prior-β grains, more uniform α-lath widths, and more-uniform microhardness values within a deposited component.

2. Experimental methodology

Experiments were conducted to assess the impact of the developed controller on deposition macrostructure, microstructure, and microhardness. Deposits were made with both uncontrolled (i.e. purely feed-forward) and controlled processing parameters. Details of the experiments follow.

2.1. Physical setup and parameters

Experiments were conducted with an Optomec LENS® MR-7, laser-based, DED system (subsequently referred to as LENS). The system used a 500 W, Ytterbium-doped fiber laser (IPG YLR-500-SM). The laser fiber was coupled to a 200 μm, multimode optical fiber and focused to a D4σ (second moment) spot size of 0.624 ± 12 μm, measured using a PRIMES GmbH FocusMonitor device. As shown in Figs. 1 and 2, the focused beam exited the laser head through a coaxial, center-purge nozzle. Through the center purge nozzle, 30 lpm of argon gas flowed, coaxially, out of a 6.35 mm diameter orifice and toward the substrate below. Around the coaxial nozzle were four, radially symmetrically oriented, powder-delivery nozzles through which 4 lpm of argon gas carried a 3 g/min flow of metal powder out of a 1.19 mm orifice.

The LENS processing chamber was filled with argon gas and maintained at a gauge pressure between 498 and 748 Pa (2–3 in. of water). Oxygen levels were kept below 20 ppm during processing.

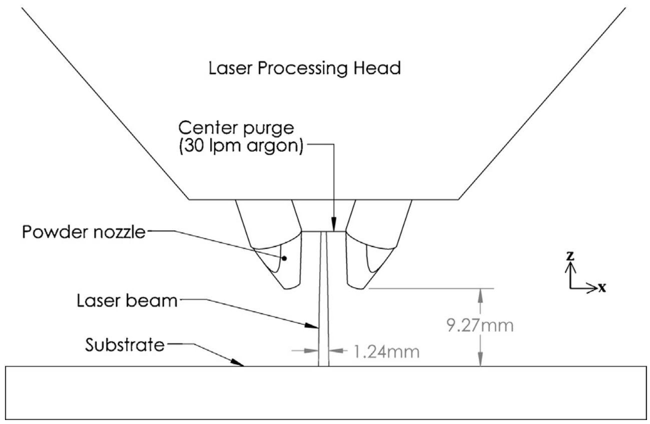

Fig. 1. Experimental setup on the laser-based, directed-energy-deposition system (Optomec, Inc. LENS).

A substrate was positioned at the working distance of 9.27 mm below the powder-delivery nozzles. At this position, below the laser focal point, the laser was defocused to a spot size of 1.24 mm. During deposition, the substrate was translated in the *X*–*Y* plane while the laser processing head remained stationary. Upon completion of a layer, the laser head moved upwards by a predefined layer height. Stage motion was controlled by a Galil DMC-1880 Motion controller. Stage position error was less than 10 μm.

During deposition, part temperature was monitored using a Raytek GPSCFLW series, single-wavelength pyrometer. A constant emissivity value of 0.40 was assumed – this was a rough estimate based on the results of Hagqvist et al. [32] and correlation with thermocouple measurements. The pyrometer measured the average temperature in a 4.5 mm diameter spot around the laser position. The pyrometer outputted a 0–10 V signal which was linearly scaled with the measured temperature. Noise in the analog signal was estimated to contribute an error of ±2 °C to measured values. The temperature around the start point of each

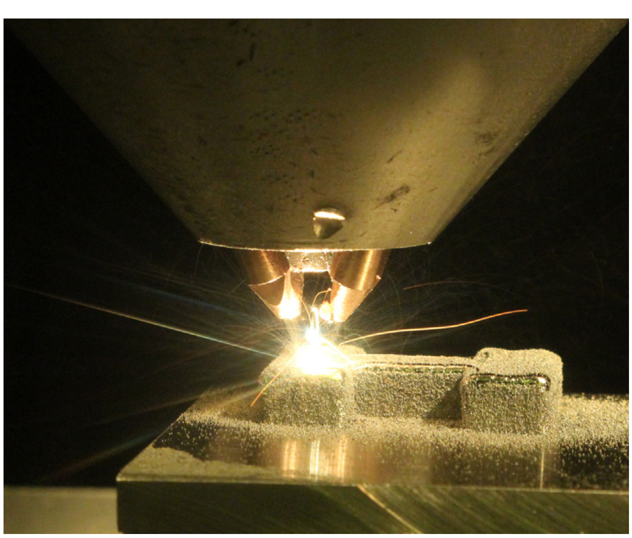

Fig. 2. Image of processes during deposition of Ti–6Al–4V within the LENS system.

potential hatch, prior to deposition, was used to actively control hatch order.

2.2. Materials

The powder used for deposition was Grade 5 titanium (Ti–6Al–4V) with extra low interstitials (ELI grade), purchased from Phelly Materials, Inc. The powder was verified to be spherical with a mean particle size of 126.8 μm (45.9 μm stdev) using scanning electron microscope imaging and a Horiba LA950 particle size distribution analyzer, respectively. Powder was deposited atop a 76.2 mm × 76.2 mm Ti–6Al–4V substrate, with a thickness of 6.35 mm.

2.3. Processing parameters

Hatching parameters were determined following the method outlined by Policelli [33]. At a measured output laser power of 450 ± 25 W and a processing speed of 10.58 mm/s (25 in./min), the geometry of single-track deposits were used to determine hatch spacing and layer thickness. To reduce the likelihood that hatch skipping would result in lack-of-fusion, the bead contact angle, with respect to the substrate, was measured and verified to be at an obtuse angle (159°). Based on this analysis, a hatch spacing of 0.91 mm (0.036 in.) and a layer thickness of 0.18 mm (0.007 in.) were used for deposition of the part geometry. It may be noted that these parameters resulted in deposition of a layer thicker than the upwards movement of the laser deposition head between layers. This overbuilding on each layer is typical in directed-energy processes and was used to ensure that the powder streams converged toward the melt pool; in the case of underbuilding, the powder would have diverged near the melt pool, resulting in little to no deposition.

2.4. Control hardware, software and dataflow

To enable real-time control of hatch order, custom software and hardware systems were integrated into the LENS machine. The system's workflow is provided in Fig. 3. First, a 3D computer-aided design (CAD) model was constructed and exported as a Standard Tessellation Language (STL) file. Next, the part orientation (build direction) was defined and the STL file was sliced into layers. Each layer was defined using a poly-line boundary representation within a common layer interface (CLI) format. These first steps, construction of the STL file, part orientation and slicing, were completed using commercial software – SolidWorks® Premium 2012 and netfabb® Studio Professional 4.

Based on the slice data, custom-written software was used to generate two sets of instructions: LENS machine code and an Additive Manufacturing Slice File (AMSF) file [34]. Machine code was formatted in the Digital Motion Controller (DMC) language, defined by Galil Motion Control, Inc. Within the DMC code, instructions defined a communication schema between the Galil motion controllers and an external computer (referred to as PSU computer). The PSU computer was equipped with a National Instruments USB 6343 multifunctional

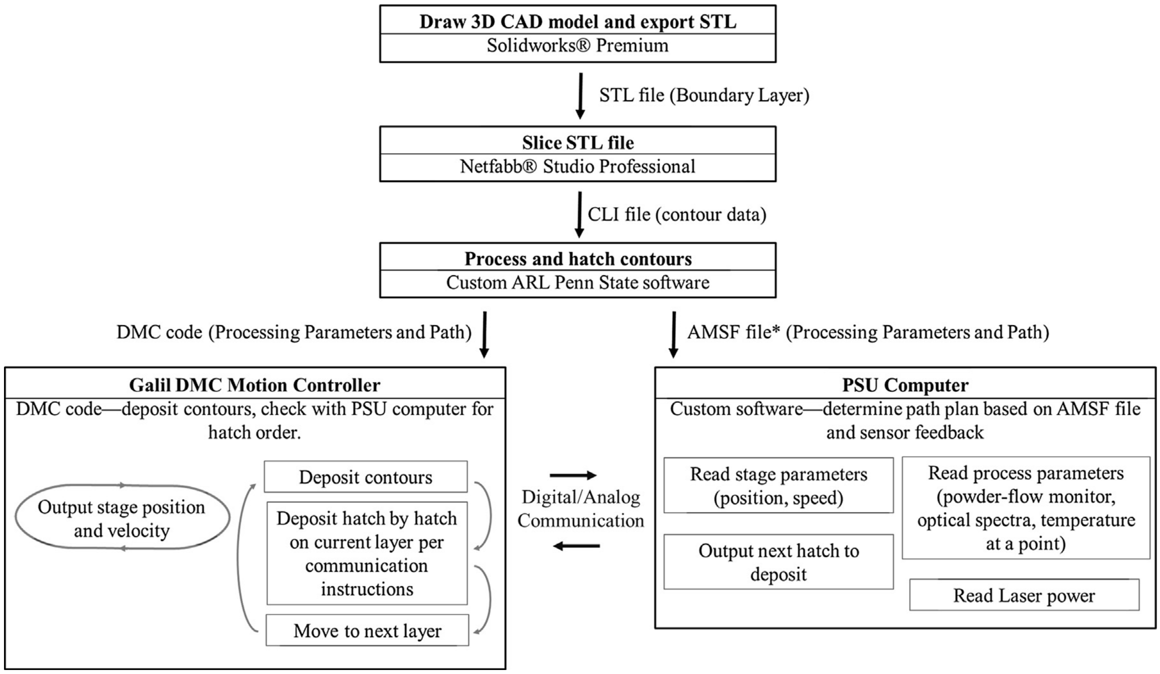

Fig. 3. Data flow for near real-time alteration of path plan. The AMSF file description can be found in Ref. [34].

Data Acquisition Device (DAQ). During processing, real-time position data were passed from the motion controller to the PSU computer using two analog (0–10 V) voltages proportional to the (*X* and *Y*-axes) stage position and digital inputs/outputs were used for hand shaking and to communicate hatch order. Analog signal noise contributed an error of less than ±17 μm in the measured position data.

On the PSU computer, custom-written software interpreted the AMSF file and read the current position, hatch, layer, pyrometer reading, and laser power. Based on these data, control decisions were made and the PSU computer communicated hatch deposition sequence in real-time to the motion controller. A diagram of the control logic is provided in Fig. 4.

Throughout the build, the time, stage positions, current hatch and layer number, pyrometer reading, and laser power were monitored by the PSU computer. Meanwhile, the motion controller was instructed to deposit all contours on each layer, check for instructions from the PSU computer and modify hatch order as directed. Each hatch was assigned an index number and assigned a threshold initial temperature. All hatches were assigned a threshold value of 415 °C. This threshold was selected for reasons of practicality – it was slightly below the saturation limit of the pyrometer at the chosen emissivity. As shown in Fig. 4, in the closed-loop build, if the initial temperature at the start point of a potential hatch exceeded the threshold value, that hatch was skipped. Then, to minimize processing time, the next closest potential hatch location was checked. On each layer, all potential hatch locations were cycled through before a previously measured hatch temperature was rechecked.

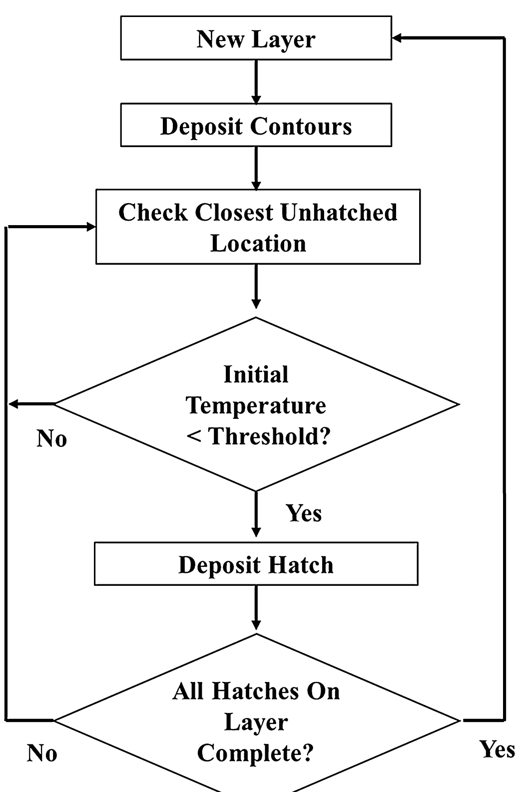

Fig. 4. Flow chart for controller logic for the closed-loop build.

2.5. Part geometry

A dogbone geometry, shown in Fig. 5, was selected in order to test the controller on a geometry with regions of varying thermal characteristics. On each layer, a contour was first deposited followed by a series of hatches. This sequence is illustrated in Fig. 6 for the uncontrolled (open-loop) build. The contour was

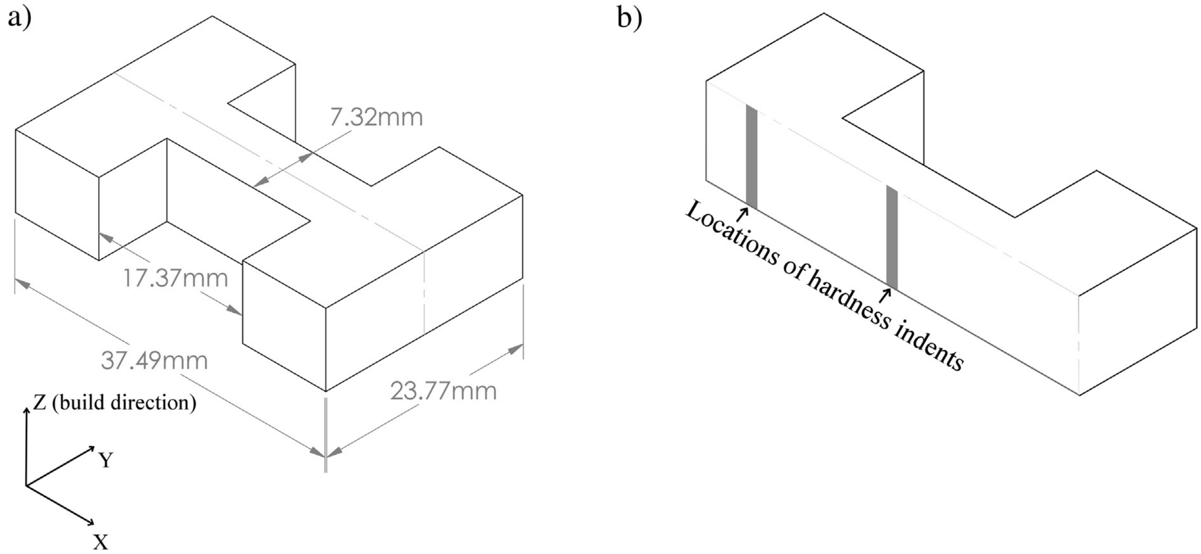

Fig. 5. (a) Build geometry. The part was cross-sectioned along the dashed gray centerline. (b) Hardness was measured along the center of the wide, left region and along the center of the narrow, middle region.

deposited along the poly-line defined by points C1,C2,. . .,Cn, shown in Fig. 6. Following deposition of the contour, hatches were deposited using a zig–zag, raster in the location and direction shown in Fig. 6. Text above each arrow in Fig. 6 indicates the order of deposited hatches. A hatch location number is located at the top of the figure. The hatch location number corresponds to each potential hatch position and is numbered sequentially along the x-axis. In the open-loop case, hatch order numbers correspond to hatch location numbers. In total, 40 hatches and 25 layers were deposited.

2.6. Characterization

Once deposited, both open-loop and closed-loop builds were cross-sectioned parallel to their length and along the centerline shown in Fig. 5. For each sample, both cross-section halves

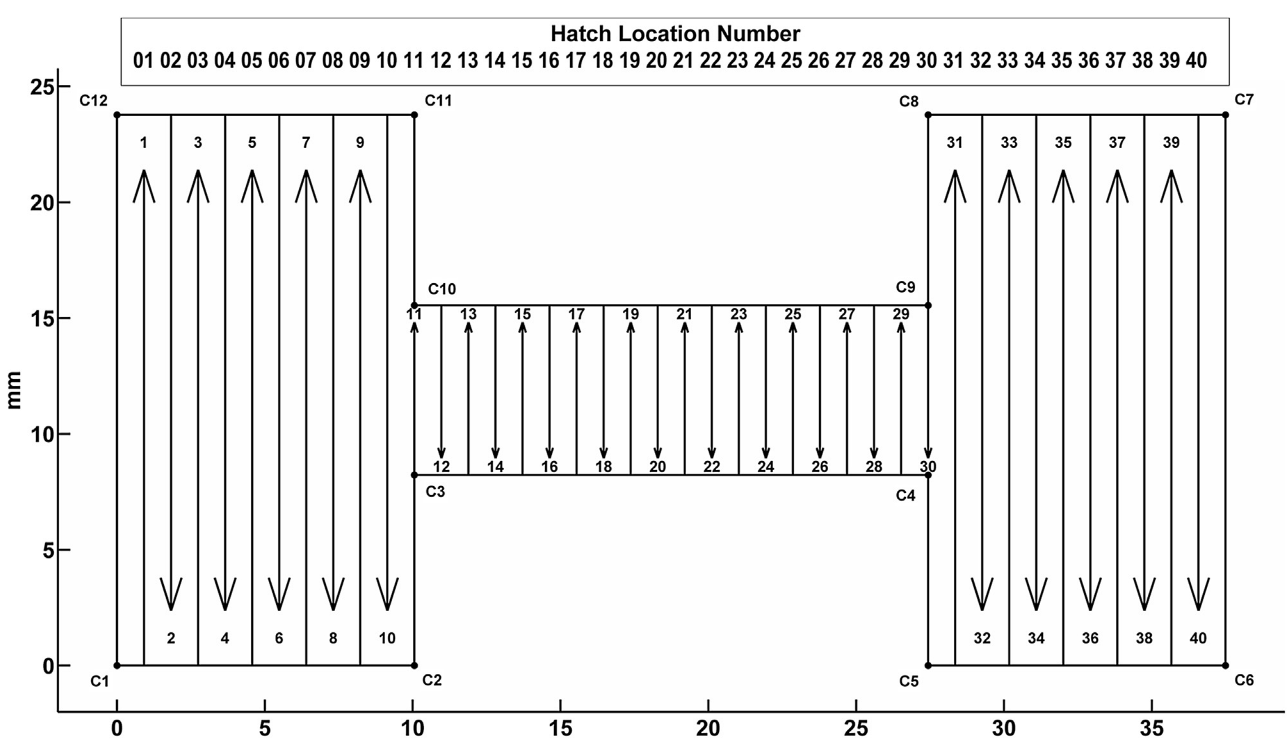

Fig. 6. On each layer, a contour, defined by points C1,. . .,Cn, was first deposited. In the open-loop build, hatches were deposited according to the order and direction shown. Hatch order numbers are located above each hatch arrow while the hatch location number is at the top of the figure. Note that the starts and ends of all hatches actually extend to contour perimeters.

were ground and polished following standard metallographic techniques. One cross-section half from each part was etched using Krolls reagent and studied using optical microscopy. On the etched cross-section, Vickers hardness was measured using a LECO-M-400-G1 hardness tester using a load of 1 kgf applied for 10 s. Hardness was measured, as a function of build height, at the two locations shown in Fig. 5(b): through the middle, narrow region and the left, wide region of the geometry. Within both regions, reported hardness values represented the average of three measurements along each depth and the standard deviation of the three measurements was represented by error bars. Unetched cross-sections were examined using a FEI Quanta 200 and a Philips XL30 environmental scanning electron microscope (SEM) in back-scattered imaging mode. From the SEM images, measurements of the α-lath widths were calculated from 20 manual measurements at random locations within each image.

3. Results and discussion

The objectives of this work were to develop an intra-layer control strategy, to assess the behavior of the control system though a case that employed temperature feedback as input to a path controller, and to determine its effects on the microstructure and hardness of the deposited part. The behavior of the system was assessed by comparing the time required to deposit all hatches on each layer, the hatch deposition order, and the initial temperatures prior to each hatch deposition. Compared to the open-loop build, the closed-loop build exhibited differences in macrostructure, microstructure, and hardness. The behavior of the control system is discussed in Section 3.1, followed by a review of macro and microstructure in Section 3.2, and the resulting microhardness along the depth of the deposited component in Section 3.3. Here, results are combined with discussion.

3.1. Behavior of control system

In the open-loop build, hatches were deposited on all layers in a sequential order as shown in Fig. 6. By the third layer, the initial temperature at the start point of most potential hatches exceeded the 415 °C threshold temperature. In the closed-loop build, the hatching sequence was significantly altered for all but the first layer.

To illustrate this, the hatching deposition sequence midway through the closed-loop build, on layer 13, is shown in Fig. 7. As in Fig. 6, the text above each arrow indicates the order of deposited hatches. The hatch location number is located at the top of the figure. Fig. 7 shows a highly active control system; on the first pass, no two hatches were deposited sequentially next to each other. On average, two hatches were skipped between each deposited hatch on this layer. This knowledge may be useful in redesigning the control algorithm; rather than checking the temperature of the nearest hatch, the total deposition time on each layer may be reduced by initially checking the second- or third-nearest hatch temperature.

Skipping of hatches which exceeded the threshold temperature is also illustrated in Fig. 8. Here, the temperature at the start of each potential hatch is shown along with the hatch location number. The threshold temperature is shown as a horizontal, dashed line and the saturation point of the pyrometer is shown as a dash-dot line.

As shown in Figs. 7 and 8, on the first pass, the temperature at the start of each potential hatch initially exceeded the threshold temperature, so the corresponding hatch was temporarily skipped. The average number of potential hatches skipped on the left, wide section of the geometry and the middle, narrow section was two. However, on the right, wide section of the geometry, only one hatch was skipped on average. Intuitively, it would be expected that, due to anticipated heat buildup, more hatches would be skipped in the middle, narrow section than on either end. However, this was not true: on average, an equal number of hatches were skipped on the left and middle sections. More hatches were also skipped on the left section than right section. The reason for this may be related to the deposition of an external contour ($C_1,C_2,\ldots,C_{13}$ in Fig. 7), at the beginning of each layer, before hatching. The contour started and ended at the left side of the geometry. Thus, the left side of the part was already hotter than the right or middle section prior to deposition of the first hatch.

The hatch order on all layers of the closed-loop build is revealed as an image plot in Fig. 9. Within the figure, the abscissa displays the layer number (1 through 25) and the ordinate displays the order of each deposited hatch (the first deposited hatch is bottommost on the axis and the last deposited hatch is topmost on the axis). The gray-scale intensity of each pixel indicates the hatch location number. As illustrated in Fig. 9, the first layer of the closed-loop build was deposited nearly in the same order as in the open-loop build – only hatches 12 and 22 were initially skipped. The number of hatches skipped on each layer increased up till the seventh layer. Beyond the seventh layer, similar patterns of skipped hatches occur on subsequent layer. Thus, the control system drove the process into steady state by the seventh layer.

The image plot of hatch sequences (Fig. 9) also reveals the number of passes (left-to-right or right-to-left hatching sequences) required to deposit each layer. Under closed-loop control, the initial temperature of each hatch was checked sequentially from left to right. Hatches with temperatures above the threshold were added to the end of the queue to be rechecked. In Fig. 9, a sequence of dark to light pixels on a layer indicates left-to right hatching along the positive *x*-axis, while a sequence of light to dark pixels indicates hatching from right-to-left hatching. Fig. 9 shows that on the first layer, only two passes were required, while beyond the second layer, six to seven passes were performed on each layer.

Hatch skipping in the closed-loop build resulted in a 33% increase is total build time compared with the open-loop build. The open-loop build was deposited in 51.56 min, while the closed-loop build was deposited in 68.53 min. The processing time for each layer, plotted in Fig. 10, shows that the layer deposition time increased with each layer, until layer 7. In contrast to the near-constant layer deposition time of 123.4 s (standard deviation of 0.6 s) in the open-loop build, each layer beyond layer seven was deposited in an average time of 166.5 s with a standard deviation of 1.5 s. The same conclusion can be drawn as

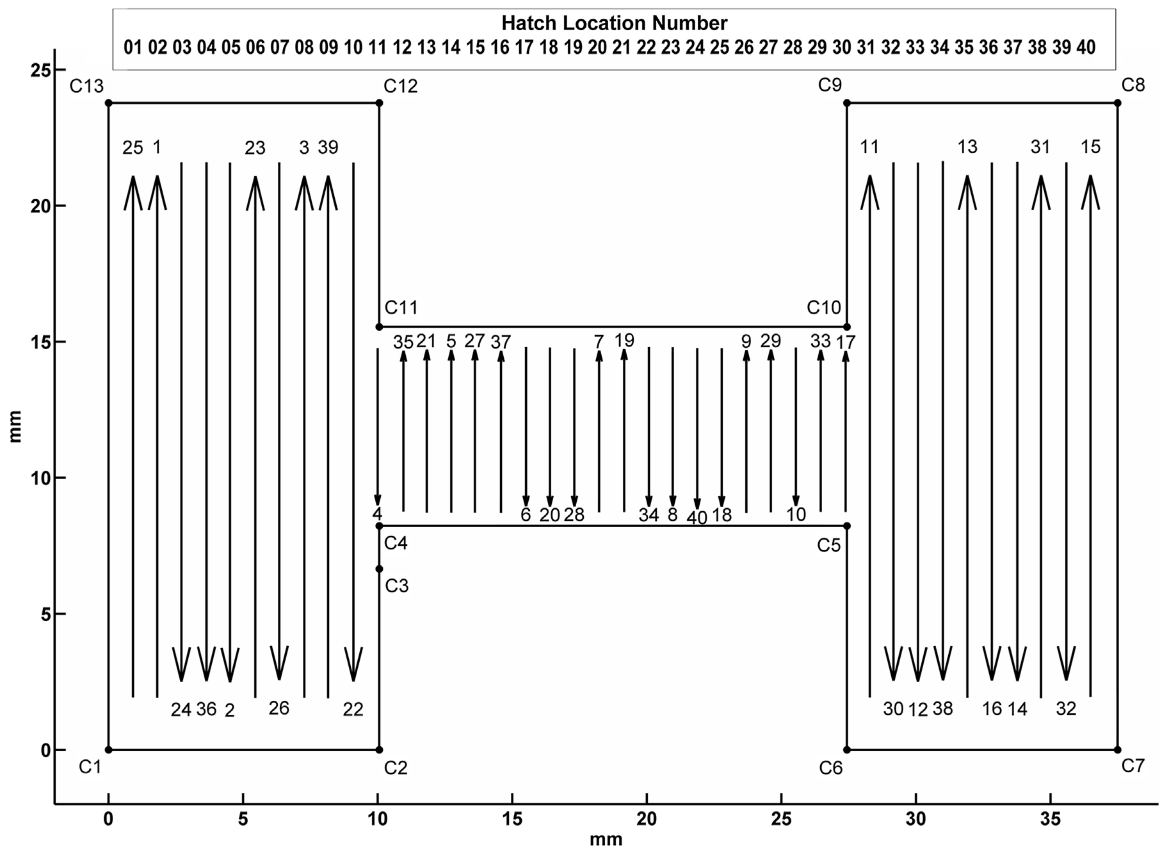

Fig. 7. Order of deposited hatches on layer 13 using closed-loop control. Arrows indicate the hatch direction while the numbers at each arrow's end indicates the order (e.g. 1 is the first deposited hatch). Hatch order numbers are located above each hatch arrow while the hatch location number is at the top of the figure. Note that the starts and ends of all hatches actually extend to contour perimeters.

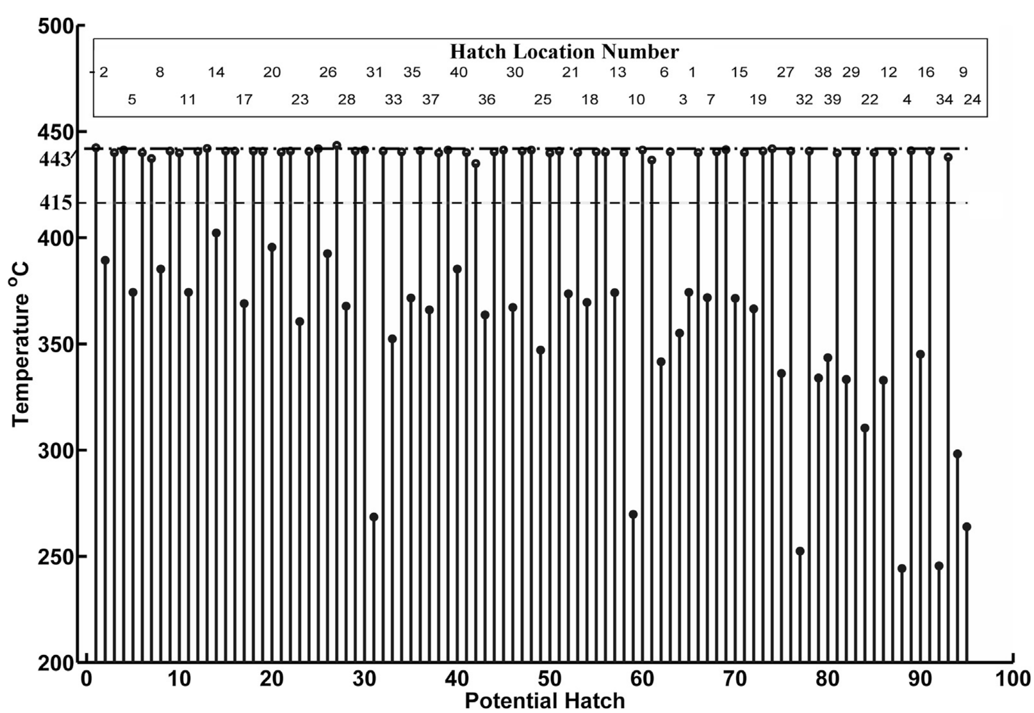

Fig. 8. Measured temperature at the start of each potential hatch on layer 13. The threshold temperature is shown as a horizontal, dashed line at 415 °C. The saturation temperature is a dash-dot line at 443 °C. The hatch location number is shown at the top of the figure.

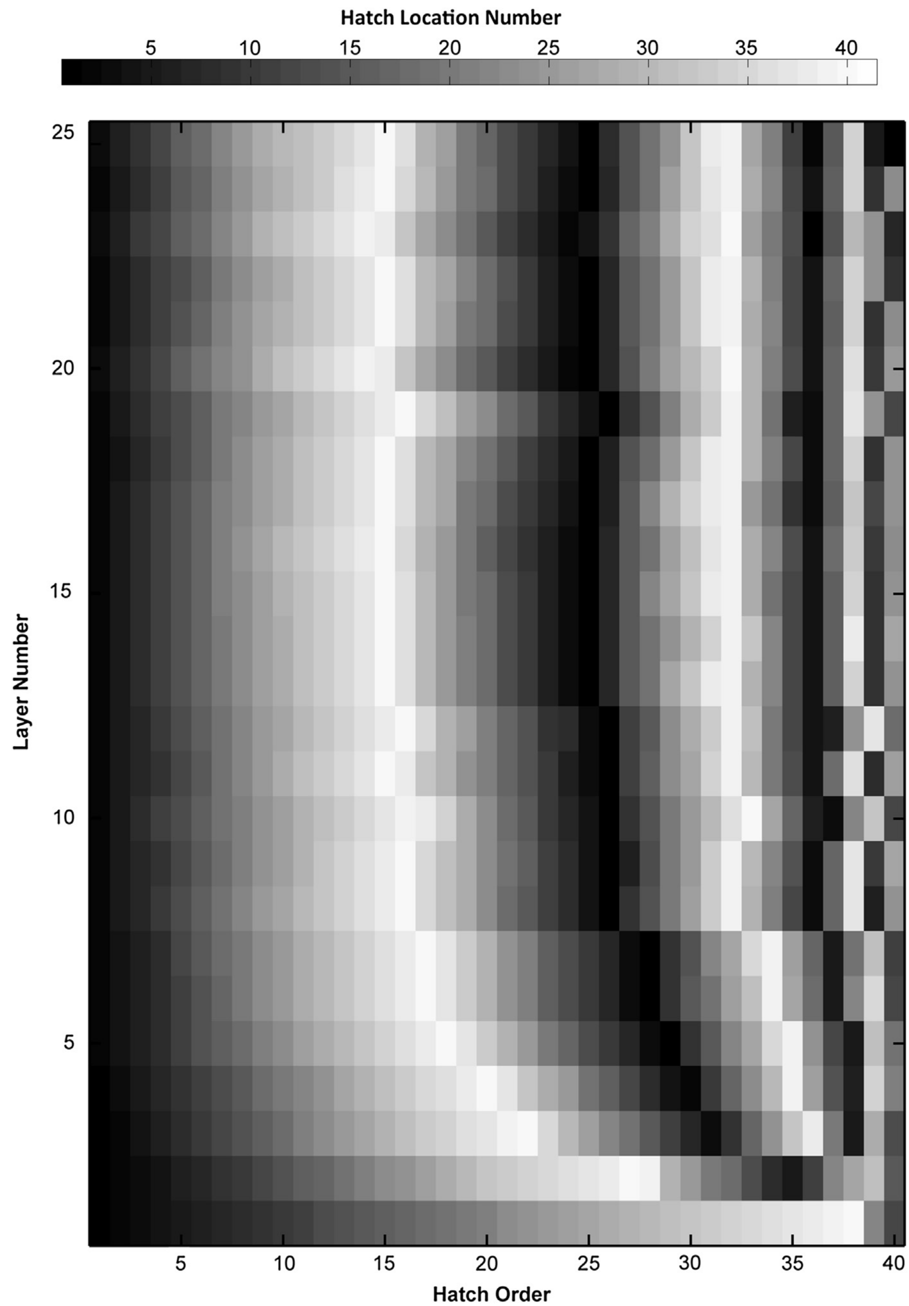

Fig. 9. This image shows the order and location of the deposited hatches, for each layer, in the closed-loop builds. The hatch location number is indicated by the gray-scale color bar. On each layer (vertical axis), the location at which a hatch was deposited can be determined by matching the hatch order (horizontal axis) with the hatch location number (top color bar).

earlier: the control system drove the processes into a near-steady state by the seventh layer.

In summary, the control system was highly active during the build. The hatching sequence was significantly altered for all but the first layer. The time to deposit each layer increased with each deposited layer until reaching a steady-state by the seventh layer. The order in which hatches were deposited similarly reached a steady-state by the seventh layer. Beyond the seventh layer, an average of two hatches were skipped on each pass. This suggests a potential improvement in the control algorithm: checking the second- or third-nearest hatch temperature rather than the temperature of the nearest hatch.

3.2. Effect of control on macro and microstructure

In both the open-loop (Fig. 11(a)) and closed-loop (Fig. 11(b)) builds, the macrostructures parallel to their length and along the centerlines, were characterized by large, columnar prior-β grains extending several millimeters in length from above the heat-affected zone (HAZ) to the top of the build. This is typical of AM Ti–6Al–4V deposits and has been explained to result from epitaxial layer-to-layer grow of β grains, from the bottom to the top of the solidifying melt pool, prior to cooling [7,8]. There was however a difference, between the open- and closed-loop builds: the orientation of prior-β grains. While

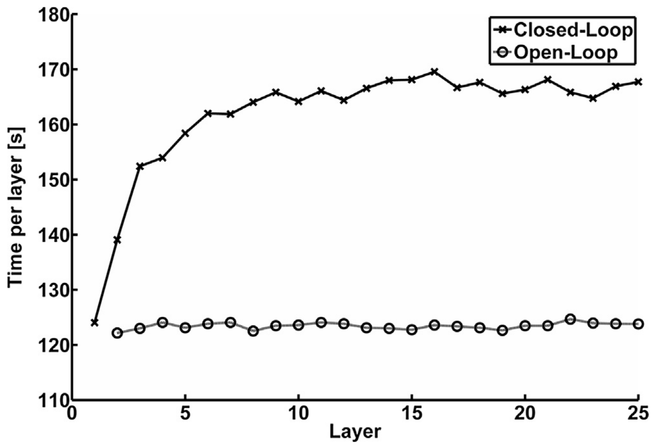

Fig. 10. Deposition time per layer for open loop (O) and closed loop (X) builds. Note that the first point in the open-loop sequence is missing due to a data-collection error on the first layer.

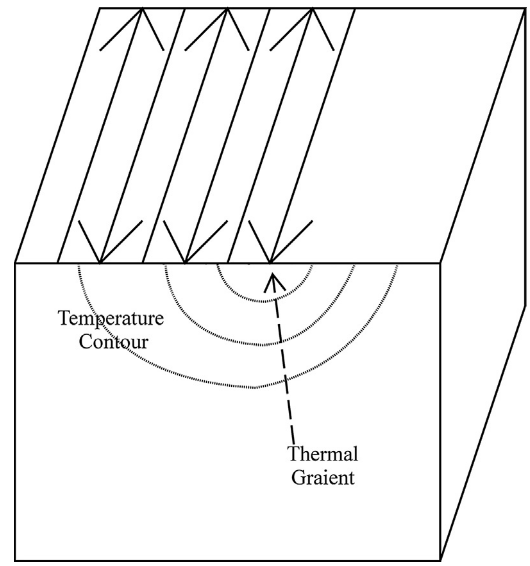

Fig. 12. Illustration of thermal gradients during sequential hatching.

columnar prior-β grains were slanted away from the vertical direction in the open-loop build, β grains were nearly vertical in the closed-loop build. This is consistent with previous observations that columnar β grains orient themselves parallel to the thermal gradient [7,8].

To explain the slanting of prior-β grains, consider an uncontrolled, sequential hatching strategy proceeding from left to right, shown in Fig. 12. Due to multiple laser passes, the temperature on the left-hand side of the last drawn hatch is higher than the substrate temperature to the right of the last hatch. Assuming cooling is dominated by conduction of heat into the part, temperature gradients can be expected to appear as sketched in Fig. 12 and the thermal gradient will be oriented down as shown in the figure. Because β grains orient themselves along the thermal gradient and grow epitaxial from layer to layer, they will appear slightly slanted in the open-loop build (Fig. 11(a)). In contrast to this, the closed-loop build required initial hatch temperatures to be below a defined threshold and resulted in multiple back-and-forth passes on each layer. Heat input was spread more uniformly on each layer and the thermal asymmetry along each side of a deposited hatch was reduced. Thus, temperature gradients were oriented perpendicular to the substrate surface, resulting in vertically aligned, rather than slanted, prior-β gains.

Within the columnar, prior-β grains, the microstructure of each build appeared to consist of fine, acicular α platelets with a small amount of intergranular β. Scanning electron microscope (SEM) images, recorded in backscattered mode, of the open-loop and closed-loop builds along the center of the middle, narrow section of the geometry, are shown in Fig. 13. Corresponding measurements of the α-lath widths, as a function of distance from the top of the deposit, are provided in Table 1. In

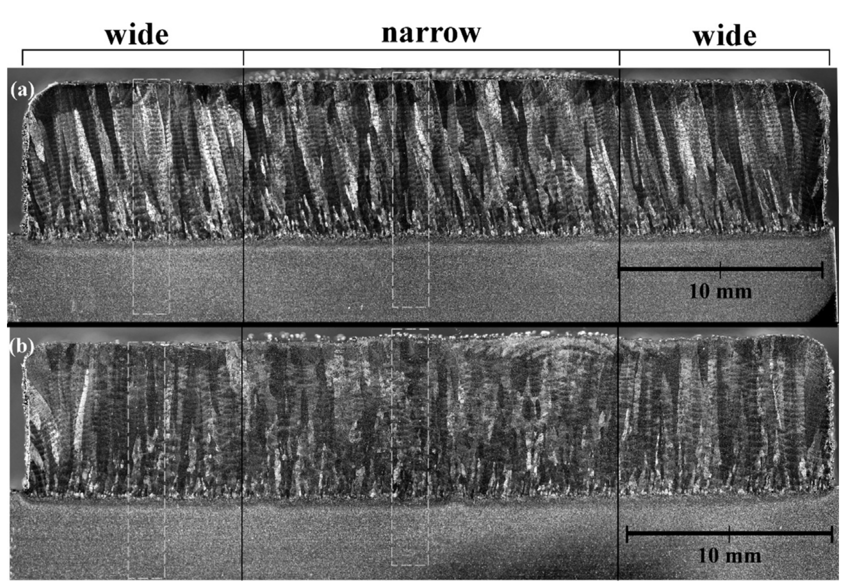

Fig. 11. Macrostructure of the (a) open-loop and (b) closed loop builds. The gray, dashed rectangles indicate the locations of hardness indents. On each build, hatching started from left to right.

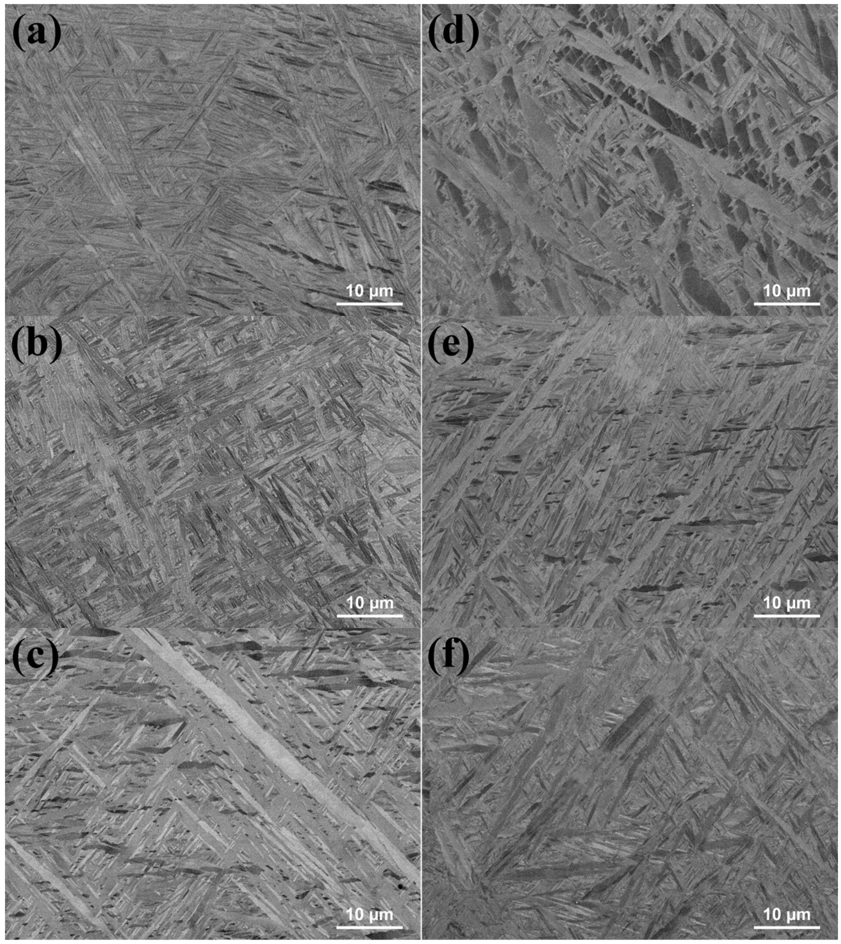

Fig. 13. Backscatter SEM images through the middle of the open-loop (a–c) and closed loop (d–f) builds. Microstructure was imaged at (a, d) 1 mm, (b, e) 4 mm, (c, f) 6 mm from the top surface of each build.

Table 1
α-Lath width through the middle of the open-loop and closed loop builds.

Distance from top (mm)	α-Lath width (μm)	Standard deviation (μm)
Open-loop		
1	0.47	0.11
4	0.63	0.13
6	0.95	0.28
Closed-loop		
1	0.29	0.07
4	0.30	0.08
6	0.33	0.08

the open-loop build (Fig. 13(a–c)), the width of α laths increased from the top to the bottom of the deposit. The change in lath width with distance from the top of the deposit was verified as statistically significant (p-value < 3.82e − 10) using an Analysis of variance (ANOVA) assuming a 95% confidence interval for the mean. In the closed-loop build (Fig. 13(d–f)), no statistically significant change in lath width with location was found (ANOVA p-value > 0.23). Average lath-widths were approximately 1.6–2.9 times smaller in the closed-loop build than in the open-loop build.

Differences in the α-lath widths between the open- and closed-loop builds can be attributed to differences in thermal conditions during the builds. Kelly and Kampe [35] have argued that wider α laths, within directed-energy deposited parts, may result from greater time above some threshold temperature below the β transus (996 °C). If correct, this may explain why the open-loop build exhibited wider α-laths and why lath width decreased with build height.

In addition to differences in α-lath width, the microstructures exhibit differences in the degree of contrast observed using backscattered electrons. As shown in Fig. 14, greater contrast was observed in the open-loop build (Fig. 14(a)) then in the closed-loop build (Fig. 14(b)). Note that contrast was enhanced in each image using contrast stretching, such that grayscale intensities were assigned linearly from the darkest to the brightest values in each the image. The greater variations in local contrast – and more clearly defined α plates – in the open-loop, compared with the closed-loop, build suggests that diffusion of alloying elements was greater in the open-loop build. We attribute this, like wider α-laths, to the greater length of time the part was exposed to some threshold temperature within the α–β phase field. A similar explanation was suggested by Griffith et al. [36] for an observed

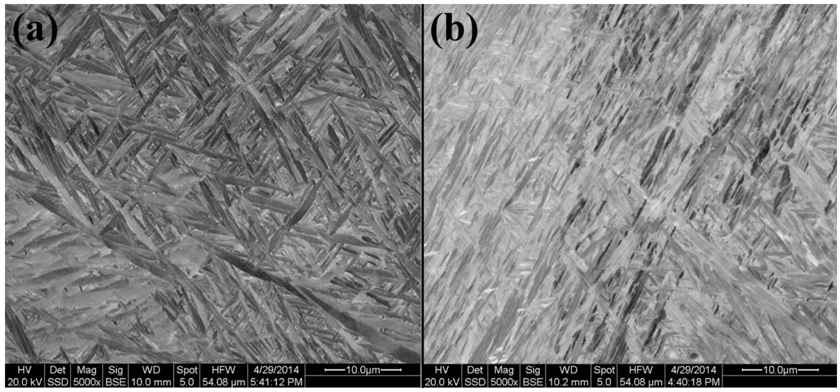

Fig. 14. Backscatter SEM images of (a) open-loop and (b) closed-loop builds taken at 4 mm from the top surface of the build. Images were recorded using the same magnification, acceleration voltage, and beam spot size. Greater contrast was observed in (a) the open-loop build then in (b) the closed-loop build, suggesting greater diffusion of alloying elements in the open-loop build.

reduction in hardness from the top to bottom of LENS-deposited of a H13 tool steel. They speculated that hardness variations were due to the tempering effect of multiple heat cycles and the resulting redistribution of carbide within the material.

3.3. Hardness

Variations in hardness were also observed between the open-loop and closed-loop builds. The hardness profile, as a function of build height, is shown in Fig. 15 for the middle, narrow region

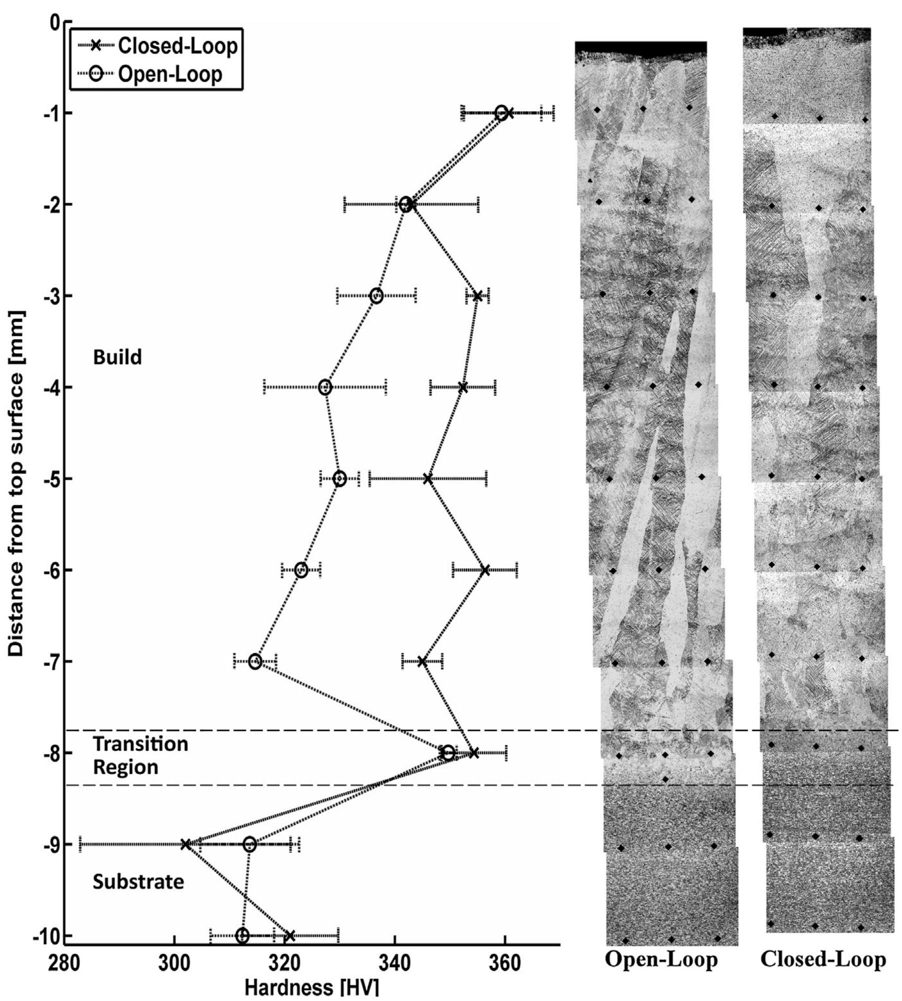

Fig. 15. The hardness profile along the middle region of the dog bone build. Approximate boundaries of the build and substrate are shown. Indents in the transition region were within the fusion zone. The sample processed with closed-loop-build-plan control was more homogeneous throughout the build than that processed without control.

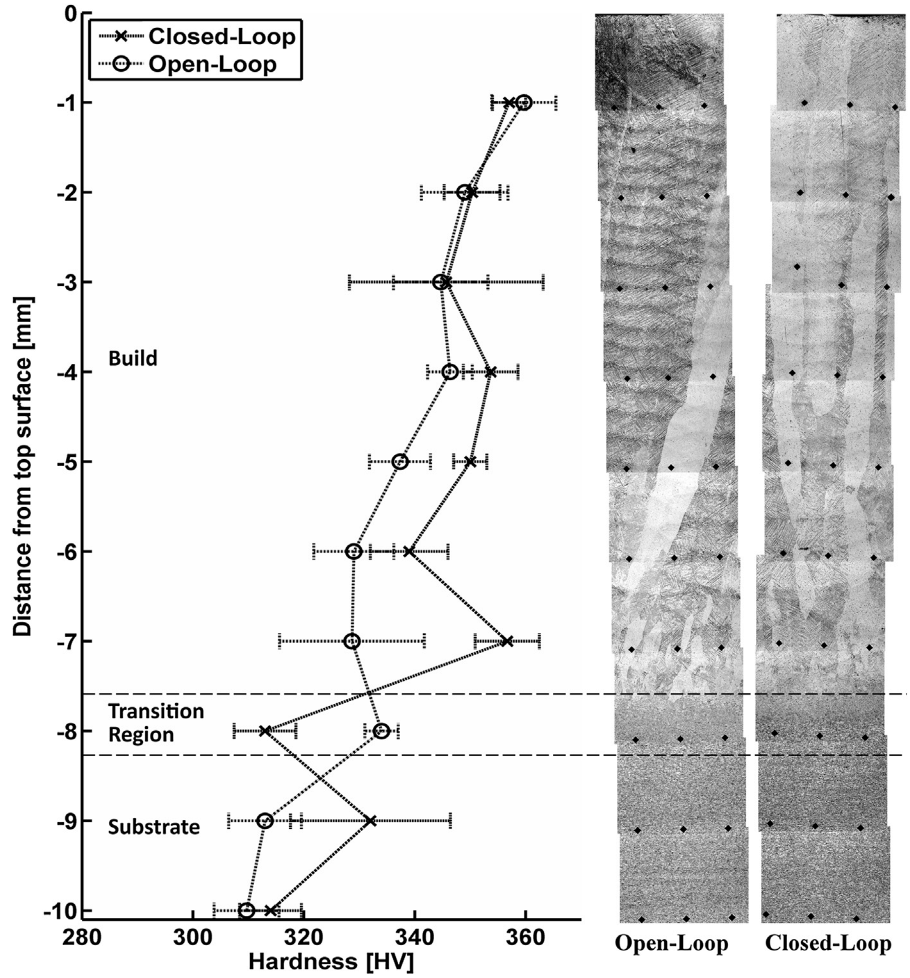

Fig. 16. Hardness along height of the left, wide region of dog bone deposit. Approximate boundaries of the build and substrate are shown. Indents within the transition region were in the heat-affected zone. The sample processed with closed-loop-build-plan control was more homogeneous throughout the build than that processed without control.

and in Fig. 16 for the left, wide region of the geometry. Through both regions, similar patterns emerged for the open-loop build: the hardness was greatest near the top surface of the build, became softer with increasing distance from the surface and then spiked in hardness within the fusion zone before reaching the substrate hardness. A similar pattern has been reported by Griffith et al. [36] for deposition of a one-bead-wide wall using H13 tool steel. In their case, the fall in hardness from the top to bottom of the build was attributed to redistribution of carbide within the material due to multiple heating cycles. Later, Costa et al. [37] demonstrated a similar pattern for a one-bead-wide deposit of AISI 420 stainless steel and showed that it could be affected by actively heating the substrate. Roy [6] also reported hardness variations between the top and bottom section of a Ti–6Al–4V part deposited using electron beam melting. Based on these reports, it appears that hardness variations with build height are a byproduct of the thermal cycling inherent in laser and e-beam AM processes.

Closed-loop control reduced the top-to-bottom variation in hardness. Through the middle, narrow region of the sample, for the open-loop build, hardness varied approximately from approximately 360 HV at 1 mm below surface of the deposit to below 315 HV at 7 mm below the surface of the build. At approximately the same coordinates in the closed-loop build, hardness varied from 360 to 345 HV. The open-loop build had significantly different (unpaired *t*-test with 95% confidence intervals, p-value = 0.002) hardness values at the surface of the build compared to 7 mm below its surface. At the same locations, the hardness values of the build produced using closed-loop control were not significantly different (p-value = 0.062). The same conclusion was drawn for the hardness through the wider, region of the samples: The hardness values of samples produced without control were significantly different ($p = 0.038$) from top-to-bottom, whereas those under closed-loop control were not significantly different (p-value = 0.935).

In addition, the hardness measured at the middle-height in both builds (the set of measurements at 4, 5 and 6 mm) was significantly different for both narrow regions ($p < 0.00001$) and wide regions ($p = 0.02438$). This difference can only be attributed to the controller. It is therefore concluded that the closed-loop build-plan controller significantly impacted microhardness and effectively reduced microhardness variations, improving overall uniformity, along the build height.

4. Concluding remarks

In this work, we introduced a system architecture to enable closed-loop control of build plan and hatch order during directed-energy additive manufacturing. To demonstrate this system architecture, a temperature-based controller was implemented and evaluated. The control system relied on tight interfacing with a commercial Optomec LENS machine and utilized a simple strategy: if the local, initial temperature of a potential hatch deposition exceeded a threshold temperature (415 °C) within the α–β phase field, it was temporarily skipped; otherwise, the hatch was deposited. This strategy resulted in control of the alignment of prior-β grains, more uniform α-lath widths, and possibly less diffusion of alloying elements within the build. In addition, uniformity of microhardness within the controlled build was enhanced.

The results indicate that intra-layer, build-plan control provides significant advantages and greater research along this direction is warranted. Additionally, controllers modeled after the one presented here offer tremendous flexibility in terms of control strategy. For instance, the threshold temperature can be specified for every possible deposition path based on heuristic knowledge or physics-based models. With slight modifications, specific paths can also be altered in mid-build, for control of macrostructure, microstructure, residual stress, distortion, and part properties. One topic of future research is how closed-loop control of path plan impacts uniformity of other physical properties, such as fatigue, elongation and strength along with potential for in-process defect corrections.

Acknowledgments

We acknowledge Mr. Edward A. Good for assistance in preparing metallographic samples. Funding for this work was provided by the Office of Naval Research, under Contract No. N00014-11-1-0668. Any opinions, findings and conclusions or recommendations expressed in this publication are those of the authors and do not necessarily reflect the views of the Office of Naval Research.

References

[1] Brandl E, Leyens C, Palm F. Mechanical properties of additive manufactured Ti–6Al–4V using wire and powder based processes. IOP Conf Ser Mater Sci Eng 2011;26:012004, http://dx.doi.org/10.1088/1757-899X/26/1/012004.

[2] Rafi KH, Karthik NV, Starr TL, Stucker BE. Mechanical property evaluation of Ti–6Al–4V parts made using electron beam melting. In: Solid free. fabr. symp. proc. Austin, TX: University of Texas; 2012. p. 526–35.

[3] Tolosa I, Garciandía F, Zubiri F, Zapirain F, Esnaola A. Study of mechanical properties of AISI 316 stainless steel processed by selective laser melting, following different manufacturing strategies. Int J Adv Manuf Technol 2010;51:639–47, http://dx.doi.org/10.1007/s00170-010-2631-5.

[4] Hrabe N, Quinn T. Effects of processing on microstructure and mechanical properties of a titanium alloy (Ti–6Al–4V) fabricated using electron beam melting (EBM), Part 2: Energy input, orientation, and location. Mater Sci Eng A 2013;573:271–7, http://dx.doi.org/10.1016/j.msea.2013.02.065.

[5] Bass BS [Master of Science] Validating the arcam EBM process as an alternative fabrication method for titanium–6Al–4V alloys. North Carolina State University; 2007.

[6] Roy L [Master of Science] Variation in mechanical behavior due to different build directions of Ti6Al4V fabricated by electron beam additive manufacturing technology. Tuscaloosa: The University of Alabama; 2013.

[7] Al-Bermani SS, Blackmore ML, Zhang W, Todd I. The origin of microstructural diversity, texture, and mechanical properties in electron beam melted Ti–6Al–4V. Metall Mater Trans A 2010;41:3422–34, http://dx.doi.org/10.1007/s11661-010-0397-x.

[8] Antonysamy AA, Meyer J, Prangnell PB. Effect of build geometry on the β-grain structure and texture in additive manufacture of Ti6Al4V by selective electron beam melting. Mater Charact 2013;84:153–68, http://dx.doi.org/10.1016/j.matchar.2013.07.012.

[9] Kruth J-P, Badrossamay M, Yasa E, Deckers J, Thijs L, Van Humbeeck J. Part and material properties in selective laser melting of metals. In: Proc. 16th int. symp. electromachining. 2010.

[10] Thijs L, Verhaeghe F, Craeghs T, Humbeeck JV, Kruth J-P. A study of the microstructural evolution during selective laser melting of Ti–6Al–4V. Acta Mater 2010;58:3303–12, http://dx.doi.org/10.1016/j.actamat.2010.02.004.

[11] Baufeld B. Effect of deposition parameters on mechanical properties of shaped metal deposition parts. Proc Inst Mech Eng B: J Eng Manuf 2011;226:126–36, http://dx.doi.org/10.1177/0954405411403669.

[12] Kobryn PA, Semiatin SL. Laser forming of Ti–6Al–4V: research overview. In: Solid free. fabr. symp. proc. Austin, TX: University of Texas; 2000.

[13] Dinda GP, Dasgupta AK, Mazumder J. Laser aided direct metal deposition of Inconel 625 superalloy: microstructural evolution and thermal stability. Mater Sci Eng A 2009;509:98–104, http://dx.doi.org/10.1016/j.msea.2009.01.009.

[14] Araujo JR, Rodriguez-Andina JJ, Farina J, Vidal F, Mato JL, Montealegre MA. FPGA-based laser cladding system with increased robustness to optical defects. In: IECON 2012 – 38th annu. conf. IEEE ind. electron. soc. 2012. p. 4688–93, http://dx.doi.org/10.1109/IECON.2012.6389491.

[15] Kruth J-P, Mercelis P, Van Vaerenbergh J, Craeghs T. Feedback control of selective laser melting. In: Proc. 3rd int. conf. adv. res. virtual rapid prototyp. 2007. p. 521–7.

[16] Bi G, Schürmann B, Gasser A, Wissenbach K, Poprawe R. Development and qualification of a novel laser-cladding head with integrated sensors. Int J Mach Tools Manuf 2007;47:555–61, http://dx.doi.org/10.1016/j.ijmachtools.2006.05.010.

[17] Hofman JT, Pathiraj B, van Dijk J, de Lange DF, Meijer J. A camera based feedback control strategy for the laser cladding process. J Mater Process Technol 2012;212:2455–62, http://dx.doi.org/10.1016/j.jmatprotec.2012.06.027.

[18] Hu D, Mei H, Kovacevic R. Closed loop control of 3D laser cladding based on infrared sensing. In: Solid free. fabr. symp. proc. Austin, TX: University of Texas; 2001. p. 129–37.

[19] Bi G, Gasser A, Wissenbach K, Drenker A, Poprawe R. Identification and qualification of temperature signal for monitoring and control in laser cladding. Opt Lasers Eng 2006;44:1348–59, http://dx.doi.org/10.1016/j.optlaseng.2006.01.009.

[20] Song L, Mazumder J. Feedback control of melt pool temperature during laser cladding process. IEEE Trans Control Syst Technol 2011;19:1349–56, http://dx.doi.org/10.1109/TCST.2010.2093901.

[21] Hand DP, Fox MDT, Haran FM, Peters C, Morgan SA, McLean MA, et al. Optical focus control system for laser welding and direct casting. Opt Lasers Eng 2000;34:415–27, http://dx.doi.org/10.1016/S0143-8166(00)00084-1.

[22] Fathi A, Khajepour A, Toyserkani E, Durali M. Clad height control in laser solid freeform fabrication using a feedforward PID controller. Int J Adv Manuf Technol 2006;35:280–92, http://dx.doi.org/10.1007/s00170-006-0721-1.

[23] Zeinali M, Khajepour A. Height control in laser cladding using adaptive sliding mode technique: theory and experiment. J Manuf Sci Eng 2010;1321:041016, http://dx.doi.org/10.1115/1.4002023.

[24] Heralić A, Christiansson A-K, Lennartson B. Height control of laser metal-wire deposition based on iterative learning control and 3D scanning. Opt Lasers Eng 2012;50:1230–41, http://dx.doi.org/10.1016/j.optlaseng.2012.03.016.

[25] Song L, Bagavath-Singh V, Dutta B, Mazumder J. Control of melt pool temperature and deposition height during direct metal

deposition process. Int J Adv Manuf Technol 2011;58:247–56, http://dx.doi.org/10.1007/s00170-011-3395-2.

[26] Muller P, Mognol P, Hascoet J-Y. Modeling and control of a direct laser powder deposition process for Functionally Graded Materials (FGM) parts manufacturing. J Mater Process Technol 2013;213:685–92, http://dx.doi.org/10.1016/j.jmatprotec.2012.11.020.

[27] Carvalho PA, Braz N, Pontinha MM, Ferreira MGS, Steen WM, Vilar R, et al. Automated workstation for variable composition laser cladding – its use for rapid alloy scanning. Surf Coat Technol 1995;72:62–70, http://dx.doi.org/10.1016/0257-8972(94)02333-L.

[28] Boddu MR, Landers RG, Liou FW. Control of laser cladding for rapid prototyping – a review. In: Solid free. fabr. symp. proc. Austin, TX: University of Texas; 2001. p. 6–8.

[29] Reutzel EW, Nassar AR. A survey of sensing and control for metal-based additive manufacturing. In: Solid free. fabr. symp. proc. Austin, TX: University of Texas; 2014.

[30] Steen WM, Mazumder J. Laser automation and in-process sensing. In: Laser material processing. London: Springer; 2010. p. 485–518.

[31] Sun A, Kannatey-Asibu Jr E, Gartner M. Sensor systems for real-time monitoring of laser weld quality. J Laser Appl 1999;11:153–68, http://dx.doi.org/10.2351/1.521893.

[32] Hagqvist P, Sikström F, Christiansson A-K. Emissivity estimation for high temperature radiation pyrometry on Ti–6Al–4V. Measurement 2013;46:871–80, http://dx.doi.org/10.1016/j.measurement.2012.10.019.

[33] Policelli M [B.S.] Development of a New Method to Fabricate Titanium Metal Matrix Composites viaLENS with Improved Material Properties. The Pennsylvania State University; 2011. https://scholarsphere.psu.edu/files/9880vs30g

[34] Nassar AR, Reutzel EW. A proposed digital thread for additive manufacturing. In: Solid free. fabr. symp. proc. Austin, TX: University of Texas; 2013.

[35] Kelly SM, Kampe SL. Microstructural evolution in laser-deposited multilayer Ti–6Al–4V builds: Part I. Microstructural characterization. Metall Mater Trans A 2004;35:1861–7, http://dx.doi.org/10.1007/s11661-004-0094-8.

[36] Griffith M, Schlienger ME, Harwell LD, Oliver MS, Baldwin MD, Ensz MT, et al. Thermal behavior in the LENS process. In: Solid free. fabr. symp. proc. Austin, TX: University of Texas; 1998.

[37] Costa L, Vilar R, Réti T. Simulating the effects of substrate pre-heating on the final structure of steel parts built by laser powder deposition. In: Solid free. fabr. symp. proc. Austin, TX: University of Texas; 2004. p. 643–54.